

Test of non-Newtonian gravitational forces at micrometer range with two-dimensional force mapping

Jianbo Wang,¹ Shengguo Guan,^{1,2} Kai Chen,¹ Wenjie Wu,¹ Zhaoyang Tian,¹ Pengshun Luo,^{1,*}
Aizi Jin,³ Shanqing Yang,¹ Chenggang Shao,¹ and Jun Luo^{1,4,†}

¹MOE Key Laboratory of Fundamental Quantities Measurement, School of Physics,
Huazhong University of Science and Technology, Wuhan 430074, China

²College of Physics and Communication Electronics, Jiangxi Normal University,
Nanchang 330022, China

³Beijing National Laboratory for Condensed Matter Physics, Institute of Physics,
Chinese Academy of Sciences, Beijing 100190, China

⁴Sun Yat-sen University, Guangzhou 510275, China

(Received 2 October 2015; published 22 December 2016; corrected 22 May 2018)

We report an isoelectronic test of non-Newtonian forces at micrometer range by sensing the lateral force between a gold sphere and a density modulation source mass using a soft cantilever. Two-dimensional (2D) force mapping, in combination with *in situ* topographic imaging, is applied to verify the isoelectronic property of the surface. The force signal is found to be electrostatic force dominated, which is correlated with the density modulation structure for thinner gold coating and reduced by thicker gold coating and thermal annealing. Maximum likelihood estimation is used to extract the constraint on the hypothetical force based on the 2D data, and the experiment sets a constraint on the Yukawa type forces without subtraction of the model dependent force background. This result would be a meaningful complementary to previous tests with different methods.

DOI: [10.1103/PhysRevD.94.122005](https://doi.org/10.1103/PhysRevD.94.122005)

I. INTRODUCTION

In an effort to unify gravity with the other three fundamental forces, many theoretical models have predicted the existence of non-Newtonian gravitational forces at sub-millimeter range [1–8]. These have inspired a series of experiments to search for the deviation from Newton's inverse square law [9–27]. The experimental results are usually parametrized by a Yukawa type potential between two masses m_1 and m_2 at a separation r ,

$$V(r) = -\frac{Gm_1m_2}{r}(1 + \alpha e^{-r/\lambda}), \quad (1)$$

as predicted by some of the theories. Here G is Newton's universal gravitational constant, α is the relative interaction strength as compared to the Newtonian gravitational potential and λ is the interaction range.

The experiments based on torsion balance have achieved very high sensitivity and set the strongest bounds on α with λ from several tens of micrometer to millimeter range [21,22,24,27]. On the other hand, the experimental tests at micrometer range give much weaker constraints on α . This is partially due to the exponential decay of the Yukawa force, thus only a thin layer of mass on the order of λ effectively attends for the interaction. A further challenge is the intervening of the strong Casimir force and electrostatic

force background. The current constraints at this range were mostly derived from the precision measurements of the Casimir force [9–14,28–30]. However, the reliability of this method depends on the theoretical calculation of the Casimir force and the evaluation of the patch electrostatic force, both of them are still under debate [11,12,28,31–37]. A natural thought to avoid these issues is to perform a test using a density modulation source mass with an isoelectronic surface. Decca *et al.* had the first try by measuring the force difference between a test mass and source masses with different mass densities [16]. Since the thickness of the two source masses is not the same, a small ~ 3 nN signal appears due to the distance dependence of the Casimir force. Recently, they reported a new isoelectronic experiment and improve the limit by a factor of 10^3 at $\lambda \sim 300$ nm [17].

In this paper we report a different experiment of isoelectronic test of non-Newtonian forces at micrometer range. Except for using a density modulation source mass, we measure the lateral force between the test mass and the source mass to minimize the contribution of the force background dominated in normal direction. 2D force mapping is used to study the effect of different treatments on the source mass and the correlation between the signal and the modulation structure. Maximum likelihood estimation is used to set a constraint on the hypothetical forces based on the 2D data.

The paper is organized as follows. Section II describes the experimental scheme. Section III describes the experimental details, including the apparatus, the test mass and

*pluo2009@hust.edu.cn
†junluo@hust.edu.cn

cantilever, fabrication of the source mass, separation and alignments between the masses. In Sec. IV, the force sensitivity is discussed and 2D mapping data are present. The constraint on the hypothetical forces is derived with the maximum likelihood estimation. Finally, the conclusions are presented in Sec. V.

II. EXPERIMENTAL SCHEME

The experimental design is schematically presented in Fig. 1(a), where the lateral force between a test mass and a density modulation source mass is measured. The test mass is a gold sphere attached to the end of a soft cantilever. The cantilever is placed normal to the source mass surface so that it is sensitive to the lateral force. The source mass is made of alternative high density (gold) and low density (silicon) materials and thus produces a spatially modulated gravitational field in either Newtonian or non-Newtonian origin. However, the Newtonian gravitational force is out of our concern as it is much smaller than the instrumental sensitivity. By driving the source mass oscillating along the x -direction with a piezo, a time-varying lateral force exerts on the gold sphere and then bends the cantilever periodically. The displacement of the cantilever is measured with a home-made fiber interferometer [38] and then the force is measured. The source mass is coated with a layer of gold film to make its surface isoelectronic, so that the electrostatic force and Casimir force are in principle constant at constant separation. As the probe is sensitive to the lateral force, the effect of the forces dominated in the normal direction is further reduced.

For a force $F(x, y)$ varying in a plane, if the source mass oscillating as $x_0 + A_d \cos(2\pi f_d t)$, the harmonic signal measured is given by:

$$F_{2n}(x_0, y_0) = \frac{1}{\pi} \int_0^{+\infty} (-1)^n \text{Re}[F(k, y_0) e^{ikx_0}] J_{2n}(kA_d) dk, \quad (2)$$

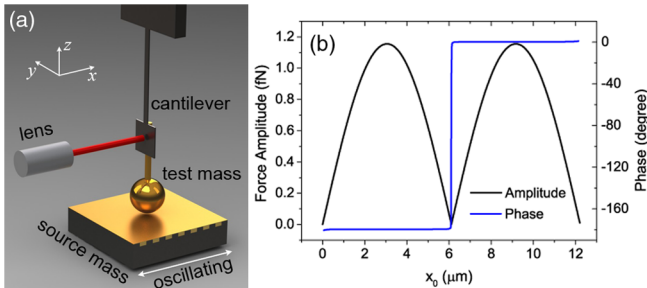


FIG. 1. (a) Schematic drawing of the experiment. Dimensions are not in scale. (b) Theoretical prediction of the Yukawa force at $8f_d$ as a function of the equilibrium position x_0 for $\alpha = 1 \times 10^{10}$, $\lambda = 1 \mu\text{m}$. The phase shows that the signal is either in-phase or antiphase with the drive signal.

$$F_{2n+1}(x_0, y_0) = \frac{1}{\pi} \int_0^{+\infty} (-1)^{n+1} \text{Im}[F(k, y_0) e^{ikx_0}] \times J_{2n+1}(kA_d) dk, \quad (3)$$

where $F(k, y_0)$ is the Fourier transformation of $F(x, y_0)$, and $J_n(kA_d)$ is the n th-order Bessel function, (x_0, y_0) is the equilibrium position of the source mass with respect to the test mass, A_d and f_d are the drive amplitude and frequency respectively. With a optimal drive amplitude, the Yukawa force signal is expected to be significant at the 8th harmonics of the drive frequency. It is also worth noting that the harmonic signal is in principle always real according to Eq. (2) and Eq. (3). That means the force signal is either in-phase or antiphase with respect to the drive signal as demonstrated in Fig. 1(b), where the calculated force as a periodic function of x_0 is presented.

III. EXPERIMENTAL DETAILS

A. Apparatus

The measurement has been performed on a custom built ultra-high-vacuum (UHV) scanning probe microscope (SPM). The system consists of a load-lock chamber and two UHV chambers: the preparation chamber and the SPM chamber with a base pressure down to 4×10^{-10} mbar. The preparation chamber is installed with an ion sputtering gun for surface cleaning and a thermal evaporator for gold film deposition. The measurement is performed with a scanning probe microscope installed in the SPM chamber. The test mass or source mass can be transferred between the chambers without breaking the vacuum. The whole system is rested on four pneumatic isolators serving as the first-stage vibration isolation.

The microscope head is composed of a fiber probe stage, a source mass stage and a probe stage, which are screwed on a titanium frame [see Fig. 2(a)]. The head is suspended through three springs inside the vacuum chamber for second-stage vibration isolation. The fiber stage, which can translate along the x -, y - and z -axis, is used to align the focus of the laser beam to the center of the reflective pad of the cantilever.

The source mass stage consists of a set of positioners (attocube systems AG) and a sample socket mounted on top of them. Three positioners, two for the x -, y - directions and one for the z - direction, are used for coarse movement. A xyz scanner is mounted on top of those positioners for x , y , z fine displacement. Another linear scanner (x scanner) with a maximum travel range of $80 \mu\text{m}$ at room temperature is mounted on top of the xyz scanner to drive the source mass oscillating. Subsequently, a goniometer is used to adjust the surface level with a minimum step of $2 \mu\text{rad}$. On top of the goniometer, the sample socket is finally mounted.

In order to exchange probes *in situ*, a probe stage is designed and machined from a piece of titanium with a

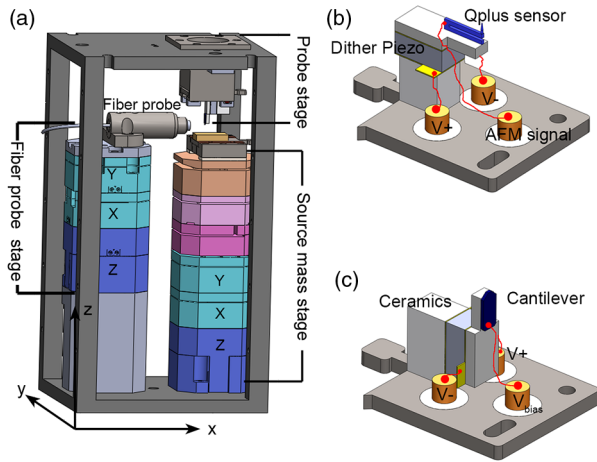


FIG. 2. Design of the scanning probe microscope head. (a) From bottom to top, the fiber probe stage includes three linear positioners in the z -, x - and y - directions. In the source mass stage, from bottom to top there are three linear positioners in the z -, x - and y - directions, a xyz scanner, a x scanner and a goniometer (rotate about the y -axis). (b) The probe plate for q Plus sensor. (c) The probe plate for cantilever.

socket to accept the probe. Two kinds of probes are used. For non-Newtonian force experiment, we use a cantilever with a gold sphere attached [Fig. 2(c)]. The displacement of the cantilever is measured with the fiber interferometer through the fiber probe. In atomic force microscopy (AFM) mode, a q Plus sensor [39] is used to image the source mass surface *in situ*.

B. Test mass and cantilever

The gold sphere was made by melting a $10\ \mu\text{m}$ in diameter high purity gold wire (99.99% in purity, Goodfellow) using hydrogen flame. The sphere is naturally formed by surface tension. To keep the gold sphere pristine, extra attention has been paid to avoid any contact with the sphere surface. The gold sphere is cut from the gold wire with a tail left that serves as a handle for manipulation. The gold sphere was then glued to the end of a soft cantilever under an optical microscope. To have a low spring constant, the commercial silicon nitride cantilever with nominal thickness of $200\ \text{nm}$ was resized by a focused ion beam to a $76.6(4)\ \mu\text{m}$ by $5.2(2)\ \mu\text{m}$ beam and a $27.2(3)\ \mu\text{m}$ by $24.6(3)\ \mu\text{m}$ reflective pad. The electrical conduction to the sphere is realized by coating the sphere-cantilever assembly with $20\ \text{nm}$ thick gold film on both sides. The dimensions of the assembly were measured by scanning electron microscopy (SEM) (see Fig. 3). The gold rod is $145(2)\ \mu\text{m}$ long with a diameter of $8.8(3)\ \mu\text{m}$. The sphere radius is measured to be $13.7(1)\ \mu\text{m}$.

C. Source mass

The density modulation source mass was fabricated on a silicon-on-insulator (SOI) wafer, where a $60\ \text{nm}$ buried

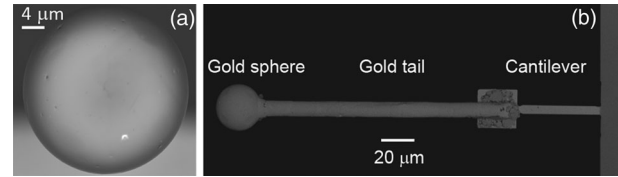


FIG. 3. SEM images of (a) the gold sphere (bottom view), (b) the assembly of the test mass and the cantilever.

silicon oxide layer is sandwiched between a $3.3\ \mu\text{m}$ device silicon layer and a $400\ \mu\text{m}$ handle silicon layer. The device layer was first patterned to parallel trenches with a period of $12.2\ \mu\text{m}$ using lithography and deep reactive ion etching (DRIE). Each trench has a width of $6.3\ \mu\text{m}$ and a depth of $3.3\ \mu\text{m}$. The trench was then filled with gold by electroplating. Figure 4(a) presents a SEM image of the cross section after electroplating. After mechanically polishing, the electroplated surface was glued to a glass plate with optical adhesive. The handle silicon layer was then thinned down by mechanically grinding and polishing, and eventually removed by DRIE. Afterward, the silicon oxide surface is exposed. To make it isoelectronic, the exposed surface was first cleaned by ion sputtering and then coated with a layer of gold in the same vacuum system as for the measurement. The thickness of the gold coating was chosen to be $150\ \text{nm}$, $300\ \text{nm}$, $400\ \text{nm}$, and $500\ \text{nm}$. For the $500\ \text{nm}$ thick sample, thermal annealing was also performed in the preparation chamber. During DRIE, the silicon oxide serves as a stop layer for etching, which enables us to fabricate such density modulation structure with a surface of minimal memory of the underlying structure. The imprint of the modulation structure on the surface has $\sim 3\ \text{nm}$ average amplitude measured with atomic force microscopy (AFM) [Fig. 4(b)].

D. Separation and alignments

The separation between the two masses was set by retracting the source mass a certain distance away from the “soft” contact point where a tunneling current of $100\ \text{pA}$ was achieved with a bias of hundreds millivolts. The total

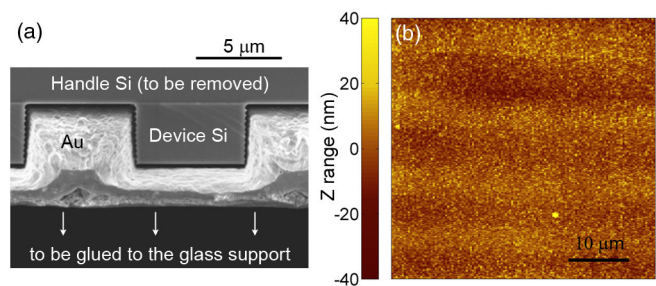


FIG. 4. (a) SEM image of the source mass cross section after electroplating. (b) AFM image taken on the source mass with $500\ \text{nm}$ thick of gold coating and then thermal annealing. Image size: $46\ \mu\text{m} \times 46\ \mu\text{m}$.

TABLE I. Table of the estimated uncertainties in determination of the separation between the test mass and the source mass for the experimental run used to set the limit on α .

Parameter	Value	Error	Units
Thickness of silicon oxide layer	51	19 ^a	nm
Thickness of gold coating	500	34	nm
Surface-to-surface separation	354	38	nm
piezo travel distance	338.3	2.3	nm
cantilever bending correction	15.3	1.8	nm
tunneling gap		1.0	nm
surface roughness ^b		8.1	nm
thermal drift		28	nm
z compensation error (x)		12	nm
z compensation error (y)		20	nm
Total distance	905	54	nm

^aThe thickness reduction due to ion sputtering clean is estimated to be 5 nm with an uncertainty of 5 nm. The possible over etching of DRIE is estimated to be 3.8 nm with an uncertainty of 3.8 nm. The uncertainty of the original thickness is 10 nm.

^bThe same surface roughness is assumed to the sphere surface.

distance between the test mass and the density modulation structure, as summarized in Table I, is the sum of the thickness of the gold coating and the silicon dioxide, the travel distance of the piezo, and the correction due to the cantilever bending when approaching the surface. The piezo travel distance is calibrated by the interferometer with a cavity formed between the fiber probe and the source mass surface through a 45° reflective mirror inserted in the probe stage. As the cantilever is away from the normal of the source mass surface by $-10(26)$ mrad, the cantilever may be bent by the electrostatic force and the Casimir force during distance setting. The separation change caused by bending is corrected through the lateral displacement measurement of the cantilever. The uncertainty of the surface-to-surface separation is also contributed from surface roughness, thermal drift, the tunneling gap, and the z compensation error in 2D force mapping.

The tilt of the source mass about the y -axis is adjusted to less than 1 mrad using the goniometer. The tilt about the x -axis has no obvious effect on the force measurement. In 2D force mapping, the separation variation due to the surface tilt is compensated by the z piezo. The rotation of the source mass about the z -axis [53(5) mrad] is measured through the topographic images. The main effect of the rotation is to slightly rescale the effective density modulation period by a factor of $1/\cos\theta$. As the cantilever is sensitive to the lateral force, the tilt of the cantilever about the y -axis and the rotation about the z -axis are easily controlled to have a negligible influence on the measurement.

During data acquisition, the source mass was driven to oscillate sinusoidally along the x -axis at $f_d = 2.1$ Hz. The drive amplitude $A_d = 18.4$ μm was chosen so that the Yukawa force signal would be significant at the 8th harmonics of the drive frequency. The separation of the

signal frequency from the drive frequency is beneficial to avoid spurious signals.

IV. EXPERIMENTAL RESULTS

A. Force sensitivity and displacement spectra

The cantilever displacement x is measured by the interferometer as $x = S_{\text{int}}V_{\text{int}}$, where S_{int} is the sensitivity at the maximum slope point of the interference pattern and V_{int} is the interferometer output signal. The displacement x as a function of angular frequency is

$$x(\omega) = \frac{1}{k} \frac{\omega_0^2}{\omega_{\text{eff}}^2 - \omega^2 + i\omega_0^2/Q_{\text{eff}}} F(\omega), \quad (4)$$

where $F(\omega)$ is the applied force. The ω_{eff} (Q_{eff}) is the effective resonant angular frequency (quality factor) modified by the optomechanical coupling, $\omega_0 = \sqrt{k/m}$ is the intrinsic resonant angular frequency, k is the effective spring constant and m is the effective mass. The intrinsic resonant frequency [$f_0 = 189.20(2)$ Hz] and quality factor [$Q_0 = 319(7)$] are obtained by measuring the laser power dependence of ω_{eff} and Q_{eff} [40].

Considering the extended mass distribution of the probe, we applied finite element analysis (FEA) to calculate the mechanical response of the cantilever. The simulation model is set as close as possible to the real structure measured by SEM. With only one tunable parameter, the cantilever thickness $t_{\text{cl}} = 216$ nm which is comparable to its nominal value, we can match the eigenfrequency of both bending modes, f_0 and f_1 , to the experimental data within 1% uncertainty [Fig. 5(a)]. The effective spring constant derived from FEA is 1.3 (2) mN/m with a uncertainty contributed from the error of the dimension measurement.

The thermal Langevin force is given by

$$F_{\text{th}} = \sqrt{\frac{2k_s k_B T_{\text{eff}}}{\pi f Q_{\text{eff}}}} \quad (5)$$

considering the internal damping in the flexible cantilever beam [41], where k_s is the effective spring constant when a force is loaded on the end of the flexible cantilever beam. The k_s is estimated to be 8.8 mN/m with FEA, different from k which is estimated with a force loaded on the end of the gold sphere [42]. The effective mode temperature T_{eff} of 8.3 K is obtained with the equipartition theorem $T_{\text{eff}} = k_s \langle x_s^2 \rangle / k_B$, where x_s is the displacement at the end of the flexible cantilever beam. We calculate the displacement thermal noise with Eq. (4) and Eq. (5) and plot in Fig. 5(b). The results are found to match with the experimental data very well around f_0 . We can see the noise level is higher than the thermal noise at lower frequency due to the $1/f$ noise from other sources. The minimum detectable force at the signal frequency ($8f_d$) is estimated to be 5.7 fN/ $\sqrt{\text{Hz}}$.

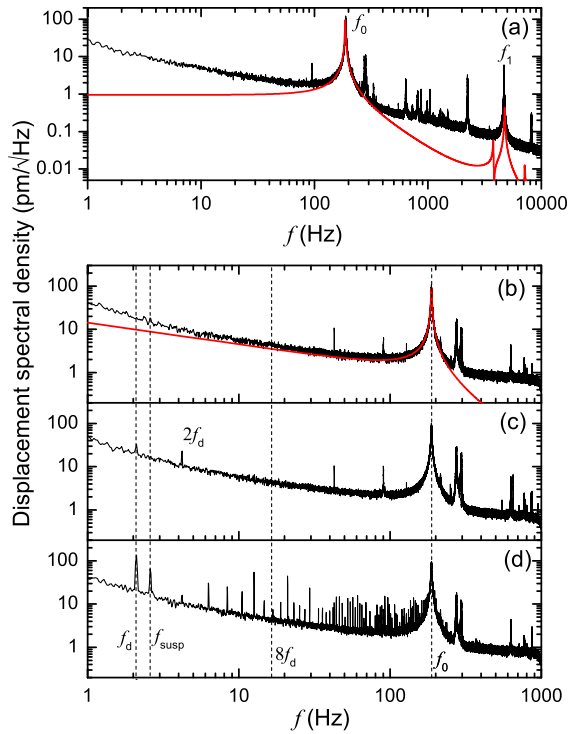


FIG. 5. (a) The displacement spectral density of the cantilever shows the transverse eigenmodes of frequency f_0 and f_1 . Other peaks in between are supposed to be related to the instability of the positioner stage. The solid line (red) is the transverse mechanical transfer function calculated by FEA with a coefficient multiplied to match the experiment. (b), (c), (d) The displacement spectral density when the source mass is (b) at rest, or oscillating at a distance of (c) $\sim 3 \mu\text{m}$, (d) 640 nm away from the test mass. The solid line (red) in (b) shows the theoretical thermal noise. f_{susp} : the resonant frequency of the suspension system of the microscope.

In Fig. 5, we also compare the displacement spectral density in three situations. When the source mass is at rest, we observe a clean noise background up to 40 Hz. By driving the source mass oscillating at a distance $\sim 3 \mu\text{m}$ away from the test mass, two peaks appear at the drive frequency and its second harmonic. These signals are expected from the vibrational coupling between the cantilever and the source mass stage, which is rapidly reduced at higher harmonics and has no contribution at $8f_d$. With the source mass further approaching to the test mass, more peaks appear at higher harmonics, which are related to the interaction between the test mass and source mass. We investigate the force signal at $8f_d$ by 2D force mapping in the following.

B. 2D force mapping

To understand the origin of the signal at $8f_d$, we took a 2D mapping of the $8f_d$ signal. In this measurement, data were taken on a grid with each grid point corresponding to an equilibrium position of the source mass. Time-series data were recorded for 22 seconds for every equilibrium

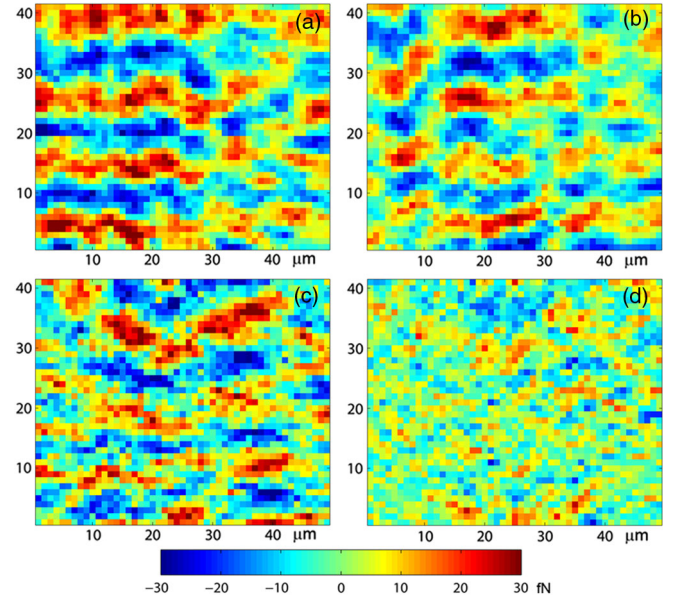


FIG. 6. 2D maps of the force signal at $8f_d$. Thickness of gold coating: (a) 150 nm, (b) 300 nm, (c), and (d) 500 nm. (d) The source mass is further annealed at 150°C for 12 hours.

position at a sample frequency of 2 kHz. During data acquisition, the test mass was electrically grounded and the residual potential difference was compensated by applying a voltage on the source mass. The in-phase and quadrature components of the signal are obtained for every grid point by Fourier transformation of the data using the drive signal as the phase reference. As indicated in Eq. (2), the $8f_d$ signal is in principal in-phase or antiphase with the drive voltage, so that the small amount of the quadrature component due to the phase delay of the electronic circuit is corrected.

Figure 6 presents the 2D images of the in-phase signal taken on the source mass after different treatments. The source masses were gradually coated with gold of thickness 150 nm, 300 nm, 400 nm (not shown in Fig. 6) and 500 nm. For 500 nm gold coating, the source mass was also annealed at 150°C for 12 hours. The 2D images show obvious spatial variation. For gold coating of 150 nm, a stripe structure is observed orientating in the same direction as the density modulation structure. The period of the stripe is comparable to the density modulation period. The result implies a correlation between the measured force and the density modulation structure. By increasing the coating thickness, we observe gradual loss of such correlation, but the image contrast remains unchanged. The standard deviation of the 2D maps stays around the same level as 12.6 fN (150 nm), 10.7 fN (300 nm), 10.6 fN (400 nm), and 12.5 fN (500 nm). It should be noted that the surface-to-surface separation decreases as we kept the distance to the modulation structure constant for those measurements. By averaging the data along the stripe direction, the thicker coating

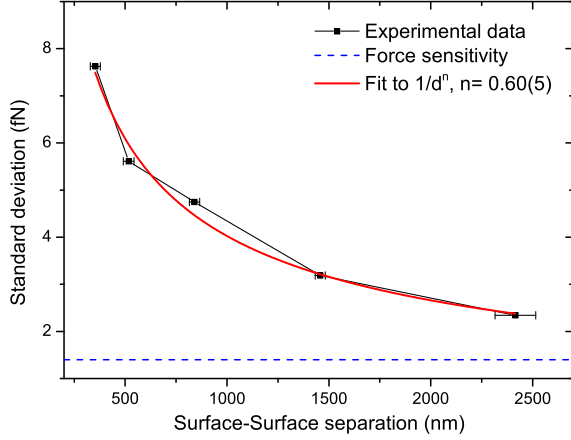


FIG. 7. Force fluctuation, represented by the standard deviation of the 2D map, is plotted as a function of the surface-to-surface separation. The force sensitivity is calculated with the data acquisition time at each grid point.

source mass gives a smaller signal than the thinner one due to less correlation with the modulation structure.

The image contrast is much reduced after thermal annealing, as demonstrated by a standard deviation of 7.6 fN. The response of the force signal to different treatments implies that a main contribution is from the electrostatic patch force. The increase of the thickness decouples the surface charge distribution with respect to the modulation structure so that less correlation is observed in thicker coating sample. The annealing process is believed to improve the homogeneity of charge distribution by increasing conductivity between gold grains.

To get further insight to it, we measured the distance dependence of the spatial fluctuation of the signal in terms of the standard deviation (Fig. 7). By fitting the data to A/d^n , we get $n = 0.60(5)$. The slower decay of the signal with distance can exclude the Casimir force as a main contribution. The amplitude of the Casimir force is also not consistent with the experiment, as estimated to be 0.65 fN

TABLE II. Table of the mean values and uncertainties of the main experimental parameters.

Parameter	Value	Error	Units
Parameters in force measurement			
Effective spring constant (k)	1.3	0.2	mN/m
Interferometer sensitivity (S_{int})	12.0	0.9	nm/V
Other parameters			
Separation (d)	905	54	nm
Test mass radius (R)	13.7	0.1	μm
Silicon mass width (W_{Si})	5.9	0.2	μm
Gold mass width (W_{Au})	6.3	0.2	μm
Electroplated gold density (ρ_{Au})	19.1	0.9	g/cm^3
Source mass depth (t)	3.3	0.1	μm
Drive amplitude (A_d)	18.4	0.1	μm
Tilt about the y -axis (θ_y)	0.0	0.7	mrad

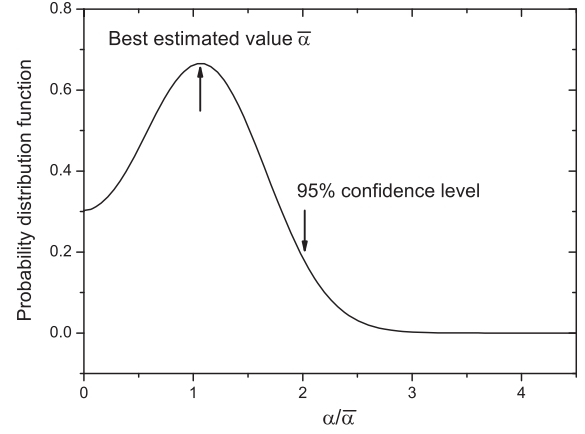


FIG. 8. Probability function as a function of α for $\lambda = 1 \mu\text{m}$.

for two ideal conductors at a separation of 400 nm using the proximity force approximation.

C. Constraint on hypothetical Yukawa force

The constraint on the hypothetical Yukawa force is obtained by maximum likelihood estimation which makes better use of the 2D data than simple average along the stripe direction. Assuming the experimental data F_{ij}^{exp} at a grid point (x_i, y_j) is a measure of the Yukawa force F_{ij}^T of α and λ with total uncertainty σ_{ij} , then the probability of occurrence is

$$P_{ij}(F_{ij}^{\text{exp}}|x_{00}, \alpha, \lambda) = \frac{1}{\sqrt{2\pi}\sigma_{ij}} e^{-\frac{(F_{ij}^{\text{exp}} - F_{ij}^T)^2}{2\sigma_{ij}^2}} \quad (6)$$

assuming Gaussian distribution is followed. The x_{00} is the offset of the source mass equilibrium position between the experiment and theoretical calculation. Considering all grid points in a 2D image, then the probability of occurrence is

$$P(F^{\text{exp}}|x_{00}, \alpha, \lambda) = \frac{1}{A} \prod_{i,j} P_{ij}(F_{ij}^{\text{exp}}|x_{00}, \alpha, \lambda), \quad (7)$$

where A is the normalization coefficient. For every λ , the best fit parameters $(\bar{x}_{00}, \bar{\alpha})$ are given by the location of the maximum probability where the experimental data matches best to the Yukawa force prediction.

The Yukawa force F_{ij}^T is calculated by numerical integration based on the experimental parameters listed in Table II. It can be written as a function of (α, x_{00}) and the experimental parameters as

$$F_{ij}^T = F_{ij}^T(\alpha, \lambda, x_i + x_{00}, y_i, A_d, d, R, W_{\text{Si}}, W_{\text{Au}}, \dots). \quad (8)$$

The total uncertainties σ_{ij} are the quadrature sum of the force measurement uncertainties and the F_{ij}^T calculation uncertainties propagated from the uncertainties of the experimental parameters. The force measurement uncertainties include

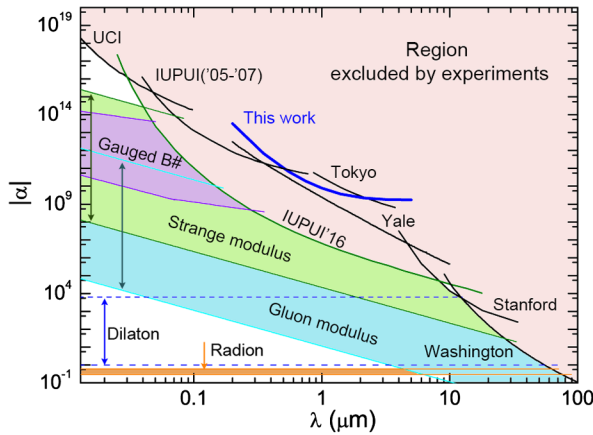


FIG. 9. Constraints on the Yukawa type forces. The heavy solid line (blue) shows result from this work. The solid lines show constraints from previous experiments [10,12–14,16,18,20,24]. Theoretical predictions [1,5,25] are also shown.

the statistics error, the uncertainty of the spring constant, and the uncertainty of the interferometer sensitivity. The random patch electrostatic force is treated here as an uncertainty in the force measurement by taking into account the standard deviation of the 2D map.

An example of the probability function is plotted in Fig. 8 as a function of α for $\lambda = 1 \mu\text{m}$. The position of maximum probability gives the best estimated α value. The constraint on the Yukawa force is set by the up-bound α value at 95% confidence level. The result, based on the data of the annealed sample, is presented in Fig. 9 with other experimental constrains and theoretical predictions. The constraint set by this work is another model-independent result obtained without subtraction of the large Casimir force and patch electrostatic force in this range.

V. CONCLUSION

The test of non-Newtonian forces at micrometer range is challenged by the dominant Casimir force and electrostatic force background. The constraints derived from the Casimir experiments rely on the correct subtraction of either or both of those force backgrounds. Isoelectronic test, as presented in this work, is a promising method to avoid such problems. To further reduce the normal force influence, we used a pendulum-like geometry where lateral force is sensed by the cantilever. 2D force mapping was first used to verify the isoelectronic property of the surface. We found that the surface quality can be improved by thicker gold coating and subsequent thermal annealing. The patch electrostatic force is found to be the main limit on current experimental sensitivity. The constraint on the hypothetical force is set by using maximum likelihood estimation based on the 2D data. The result is reliable comparing to one-dimensional measurement where under- or overestimate may happen due to the inhomogeneity of the surface. This result, obtained with a different method, would be a meaningful complementary to previous searches. With further improvement in source mass fabrication and independent characterization of patch electrostatic force, a stronger constraint may be obtained in the future.

ACKNOWLEDGMENTS

We appreciate very much Vadim Milyukov, Ho Jung Paik, and Ho Bun Chan for helpful discussion and suggestion. This work was supported by the National Basic Research Program of China under Grant No. 2010CB832802 and the National Natural Science Foundation of China under Contracts No. 11275076, No. 91436212 and No. 11305065.

-
- [1] S. Dimopoulos and G. Giudice, *Phys. Lett. B* **379**, 105 (1996).
 - [2] I. Antoniadis, S. Dimopoulos, and G. Dvali, *Nucl. Phys. B* **516**, 70 (1998).
 - [3] N. Arkani-Hamed, S. Dimopoulos, and G. Dvali, *Phys. Lett. B* **429**, 263 (1998).
 - [4] I. Antoniadis, N. Arkani-Hamed, S. Dimopoulos, and G. Dvali, *Phys. Lett. B* **436**, 257 (1998).
 - [5] S. Dimopoulos and A. A. Geraci, *Phys. Rev. D* **68**, 124021 (2003).
 - [6] T. Banks, *Nucl. Phys. B* **309**, 493 (1988).
 - [7] S. Beane, *Gen. Relativ. Gravit.* **29**, 945 (1997).
 - [8] R. Sundrum, *J. High Energy Phys.* 07 (1999) 001.
 - [9] T. Ederth, *Phys. Rev. A* **62**, 062104 (2000).
 - [10] B. W. Harris, F. Chen, and U. Mohideen, *Phys. Rev. A* **62**, 052109 (2000).
 - [11] R. S. Decca, D. López, E. Fischbach, G. L. Klimchitskaya, D. E. Krause, and V. M. Mostepanenko, *Phys. Rev. D* **75**, 077101 (2007).
 - [12] R. S. Decca, D. López, E. Fischbach, G. L. Klimchitskaya, D. Krause, and V. M. Mostepanenko, *Eur. Phys. J. C* **51**, 963 (2007).
 - [13] A. O. Sushkov, W. J. Kim, D. A. R. Dalvit, and S. K. Lamoreaux, *Phys. Rev. Lett.* **107**, 171101 (2011).
 - [14] M. Masuda and M. Sasaki, *Phys. Rev. Lett.* **102**, 171101 (2009).
 - [15] J. C. Long, H. W. Chan, A. B. Churnside, E. A. Gulbis, M. C. M. Varney, and J. C. Price, *Nature (London)* **421**, 922 (2003).
 - [16] R. S. Decca, D. López, H. B. Chan, E. Fischbach, D. E. Krause, and C. R. Jamell, *Phys. Rev. Lett.* **94**, 240401 (2005).

- [17] Y.-J. Chen, W.K. Tham, D.E. Krause, D. López, E. Fischbach, and R. S. Decca, *Phys. Rev. Lett.* **116**, 221102 (2016).
- [18] J. Chiaverini, S. J. Smullin, A. A. Geraci, D. M. Weld, and A. Kapitulnik, *Phys. Rev. Lett.* **90**, 151101 (2003).
- [19] S. J. Smullin, A. A. Geraci, D. M. Weld, J. Chiaverini, S. Holmes, and A. Kapitulnik, *Phys. Rev. D* **72**, 122001 (2005).
- [20] A. A. Geraci, S. J. Smullin, D. M. Weld, J. Chiaverini, and A. Kapitulnik, *Phys. Rev. D* **78**, 022002 (2008).
- [21] L.-C. Tu, S.-G. Guan, J. Luo, C.-G. Shao, and L.-X. Liu, *Phys. Rev. Lett.* **98**, 201101 (2007).
- [22] S.-Q. Yang, B.-F. Zhan, Q.-L. Wang, C.-G. Shao, L.-C. Tu, W.-H. Tan, and J. Luo, *Phys. Rev. Lett.* **108**, 081101 (2012).
- [23] W.-H. Tan, S.-Q. Yang, C.-G. Shao, J. Li, A.-B. Du, B.-F. Zhan, Q.-L. Wang, P.-S. Luo, L.-C. Tu, and J. Luo, *Phys. Rev. Lett.* **116**, 131101 (2016).
- [24] D. J. Kapner, T. S. Cook, E. G. Adelberger, J. H. Gundlach, B. R. Heckel, C. D. Hoyle, and H. E. Swanson, *Phys. Rev. Lett.* **98**, 021101 (2007).
- [25] E. Adelberger, B. Heckel, and A. Nelson, *Annu. Rev. Nucl. Part. Sci.* **53**, 77 (2003).
- [26] E. G. Adelberger, J. H. Gundlach, B. R. Heckel, S. Hoedl, and S. Schlamminger, *Prog. Part. Nucl. Phys.* **62**, 102 (2009).
- [27] R. Newman, E. Berg, and P. Boynton, *Space Sci. Rev.* **148**, 175 (2009).
- [28] C.-C. Chang, A. A. Banishev, R. Castillo-Garza, G. L. Klimchitskaya, V. M. Mostepanenko, and U. Mohideen, *Phys. Rev. B* **85**, 165443 (2012).
- [29] V. B. Bezerra, G. L. Klimchitskaya, V. M. Mostepanenko, and C. Romero, *Phys. Rev. D* **81**, 055003 (2010).
- [30] G. L. Klimchitskaya, U. Mohideen, and V. M. Mostepanenko, *Phys. Rev. D* **87**, 125031 (2013).
- [31] A. O. Sushkov, W. J. Kim, D. A. R. Dalvit, and S. K. Lamoreaux, *Nat. Phys.* **7**, 230 (2011).
- [32] R. O. Behunin, F. Intravaia, D. A. R. Dalvit, P. A. M. Neto, and S. Reynaud, *Phys. Rev. A* **85**, 012504 (2012).
- [33] R. O. Behunin, D. A. R. Dalvit, R. S. Decca, C. Genet, I. W. Jung, A. Lambrecht, A. Liscio, D. López, S. Reynaud, G. Schnoering, G. Voisin, and Y. Zeng, *Phys. Rev. A* **90**, 062115 (2014).
- [34] J. L. Garrett, D. Somers, and J. N. Munday, *J. Phys. Condens. Matter* **27**, 214012 (2015).
- [35] G. L. Klimchitskaya, M. Bordag, E. Fischbach, D. E. Krause, and V. M. Mostepanenko, *Int. J. Mod. Phys. A* **26**, 3918 (2011).
- [36] V. M. Mostepanenko, V. B. Bezerra, G. L. Klimchitskaya, and C. Romero, *Int. J. Mod. Phys. A* **27**, 1260015 (2012).
- [37] V. B. Bezerra, G. L. Klimchitskaya, U. Mohideen, V. M. Mostepanenko, and C. Romero, *Phys. Rev. B* **83**, 075417 (2011).
- [38] B. W. Hoogenboom, P. L. T. M. Frederix, J. L. Yang, S. Martin, Y. Pellmont, M. Steinacher, S. Zch, E. Langenbach, H.-J. Heimbeck, A. Engel, and H. J. Hug, *Appl. Phys. Lett.* **86**, 074101 (2005).
- [39] F. J. Giessibl, *Appl. Phys. Lett.* **73**, 3956 (1998).
- [40] H. Holscher, P. Milde, U. Zerweck, L. M. Eng, and R. Hoffmann, *Appl. Phys. Lett.* **94**, 223514 (2009).
- [41] P. R. Saulson, *Phys. Rev. D* **42**, 2437 (1990).
- [42] J. E. Sader, I. Larson, P. Mulvaney, and L. R. White, *Rev. Sci. Instrum.* **66**, 3789 (1995).